An Empirical Algorithm for Mitigating the Sea Ice Effect in SMAP Radiometer for Sea Surface Salinity Retrieval in the Arctic Seas

Wenqing Tang, Simon H. Yueh, *Fellow, IEEE*, Alexander G. Fore, Akiko Hayashi, and Michael Steele

***Abstract*—The L-band radiometer onboard the soil moisture active passive (SMAP) mission is used to retrieve sea surface salinity (SSS) over global ocean. In the Arctic seas, one of the major challenges of SSS remote sensing is the presence of sea ice. This paper proposes a data-driven ice correction (IC) algorithm which extracts emission from the water portion of measured brightness temperature (TB) in scenes mixed with water and ice. Emission of the ice portion was removed based on estimation according to the ice fraction (f_{ice}) in the satellite footprint and ice signature derived from surrounding pixels. The IC algorithm is applied to SMAP TB data to obtain TB with IC ($\mathrm{TB_{IC}}$), which are used for SSS retrieval using the standard JPL SMAP CAP processing system. We show that the algorithm is most effective near the ice edge, thereby increasing the $\mathrm{f_{ice}}$ threshold for possible SSS retrieval to 15% from the current 3% without IC. SMAP SSS are validated using in situ salinity collected during NASA's Ocean Melting Greenland (OMG) mission from 2016 to 2020 along the Greenland coast. The number of collocations between OMG and SMAP daily gridded salinity increased by more than 30% with IC. The statistical analysis shows a similar retrieval accuracy with or without IC, with the standard deviation of the difference between OMG and SMAP of 1.41 psu (with IC) and 1.42 psu (without IC). The bias-adjusted SMAP SSS depicts salinity patterns and gradients around Greenland consistent with OMG measurements.**

***Index Terms*—Arctic seas, sea ice, sea surface salinity, soil moisture active passive (SMAP).**

I. Introduction

ARCTIC sea ice has dramatically changed over the last few decades. Areas covered by perennial ice—ice that has survived at least one melt season—shrank from covering more than two-thirds of the surface area of the Arctic Basin in the late 1970s to about one-third now [1], [2]. In seawater opened up after seasonal ice melt, low sea surface salinity (SSS) can be a tracer for sea ice melt, river discharge, net precipitation less evaporation, or the advection of relatively low salinity waters from the south (e.g., from the North Pacific Ocean via Bering Strait) [3]–[6].

SSS fields over global oceans have been observed by three satellite missions based on L-band microwave radiometry: NASA's aquarius [7] and the soil moisture active passive (SMAP) [8], and ESA's soil moisture and ocean salinity (SMOS) [9], [10]. Although L-band sensitivity to oceanic salinity decreases in cold water (especially <5 °C) [11], satellite SSS remains valuable in monitoring Arctic SSS, supported by the finding that the variability of SSS observed in the Arctic largely exceeds the satellite SSS uncertainty ($\sim$1 psu) [12] forced by (among other things) sea ice and river discharges variability [5], [6]. Efforts have been devoted to explore the potential and improve the SSS retrieval algorithm in high latitudes, particularly for the two currently operational missions (SMAP and SMOS) [13], [14].

One of the open questions challenging SSS remote sensing in the Arctic is how to isolate and remove the effect of sea ice. Near the ice edge, space-borne radiometers likely observe a scene mixed with ice and water. (Here we focus on areas away from land so land contamination is ignored). We know that at L-band, emissivity or radiometer measured brightness temperature (TB) from the sea ice surface ($\mathrm{TB^{ice}}$) is significantly higher than from the water surface ($\mathrm{TB^{water}}$). Therefore, TB received from a footprint consisting of both ice and water ($\mathrm{TB^{meas.}}$) likely exceeds $\mathrm{TB^{water}}$, resulting in false low-SSS estimation if a retrieval algorithm designed for homogeneous seawater is used. To avoid this kind of false low signature, a rather strict ice mask or equivalent filter is applied in the current SSS retrieval algorithm. Specifically, the current SMAP SSS retrieval algorithm discards measurements if the ice fraction in the corresponding footprints exceeds 3% (JPL algorithm, [15], [16]), or 0.5% (RSS algorithm, [17]). In SMOS SSS processing, ice filtering is implicitly implemented by excluding measurements exceeding natural variability [18]–[20]. Recently, Supply *et al.* [21] presented a sea ice filtering scheme based on the pseudo-dielectric constant [22] retrieved from SMOS TB, which has enhanced capability to identify pixels "polluted" by sea ice. These ice-filtering-based approaches commonly leave a

Manuscript received May 13, 2021; revised November 7, 2021; accepted November 8, 2021. Date of publication November 11, 2021; date of current version December 6, 2021. This work was supported by the Jet Propulsion Laboratory, California Institute of Technology under a contract with the National Aeronautics and Space Administration. The work of Michael Steele was supported in part by NASA under Grant 80NSSC20K0768 and Grant NNX16AK43G, and in part by a NASA Grant to JPL via Subcontract 1587724. *(Corresponding author: Wenqing Tang.)*

Wenqing Tang, Simon H. Yueh, Alexander G. Fore, and Akiko Hayashi are with the Jet Propulsion Laboratory, California Institute of Technology, Pasadena, CA 91109 USA (e-mail: wenqing.tang@jpl.nasa.gov; simon.h.yueh@jpl.nasa.gov; alexander.fore@jpl.nasa.gov; akiko.k.hayashi@jpl.nasa.gov).

Michael Steele is with the Polar Science Center, Applied Physics Laboratory, University of Washington, Seattle, WA 98105 USA (e-mail: mas@apl.washington.edu).

Digital Object Identifier 10.1109/JSTARS.2021.3127470

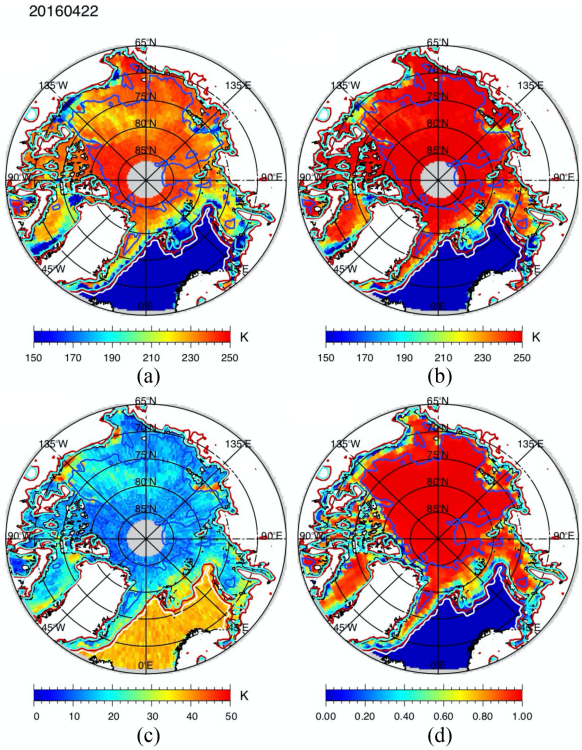

Fig. 1. SMAP brightness temperature (a) TBh, (b) TBv, (c) the polarization difference dTB = TBv-TBh, and (d) SIC north of 65°N on April 22, 2016. Contours indicate SIC values of 3% (white), red (15%), 30% (cyan), and 98% (blue).

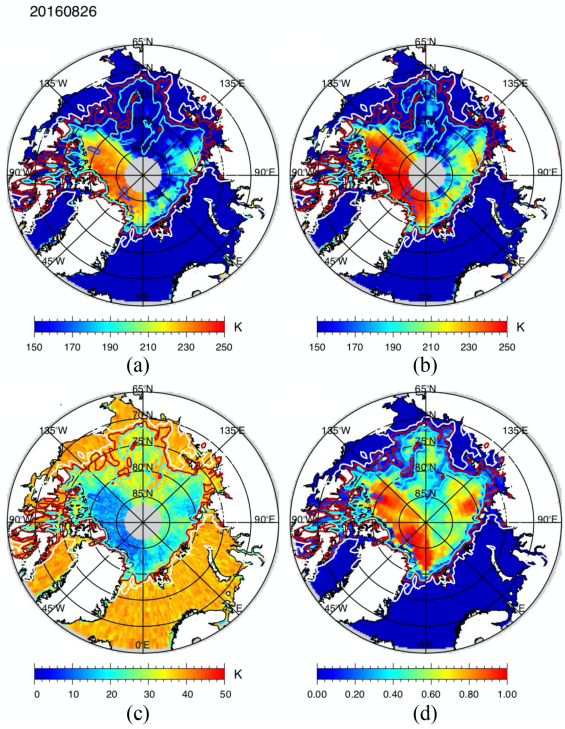

Fig. 2. Same as Fig. 1 on August 26, 2016.

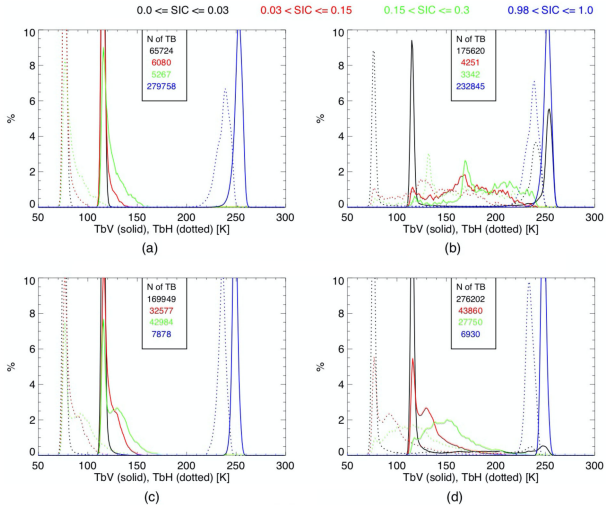

Fig. 3. Normalized distribution of SMAP TB collected north of 65°N for categories of open water (black, SIC $< 3\%$), ice edge (red, SIC 3%–15%, and green, 15–30%), and closed ice (blue, SIC $> 98\%$) on a typical day representing beginning [(a) and (b)] and end [(c) and (d)] of the ice melt season in northern hemisphere conditions by $\mathrm{SIC_{NCEP}}$ [(a) and (c)] and $\mathrm{SIC_{OSISAF}}$ [(b) and (d)]. Normalization is performed by dividing the number collected in each TB bin of size 1 K by the total number of TB in the category, which is included in the insert of each chart.

large data gap near the ice edge. However, it is the community's desire that SSS information is retrieved as close to the ice edge as possible, to facilitate understanding the linkages between oceanic processes and sea ice changes. In this study, we propose an ice correction (IC) algorithm for SSS retrieval that mitigates the ice effect in measured TB where the measurement consists of emission from both ice and water surfaces.

Over the last several decades, various techniques have been developed to separate mixed features in satellite footprints to improve the retrieval of targeted physical parameters. We considered two approaches: static or dynamic. The static approach is based on the technique of multiple endmember spectral mixture analysis (MESMA) [23], which determines the proportion in an individual pixel that is covered by a set of known types (so-called end members), which in our case include seawater, first-year-ice, multiyear-ice, etc. Analyzing SMAP measurements and collocated sea ice concentration (SIC) and ice type data, we found that MESMA was not applicable for our operational retrieval. This is mainly because the spatial/temporal variance of the sea ice surface associated with surface melting, snow covering, roughness, etc. cannot be satisfactorily determined at SMAP resolution given the uncertainty of current ice products (see Section III for details). The dynamic approach, on the other hand, extracts information needed for separating mixed features from adjacent measurements. One example of the dynamic approach is single pixel correction (SPC) [24], introduced to improve SSM/I retrieval near the coast. For each pixel of TB measured in a land/water mixed scene, SPC removes the emission from the land portion, which is proportional to the fraction of the footprint covered by the land surface (calculated for individual frequency by convolving a high-resolution land-ocean mask weighted by the antenna gain), and a representative land TB (derived as the mean of all surrounding measurements completely covered by land surface). SPC has been applied to improve retrieval in

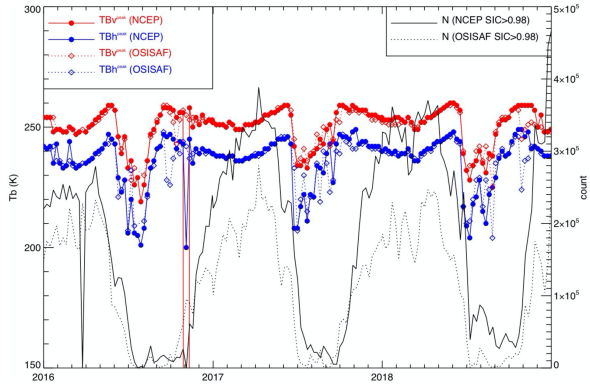

Fig. 4. Time series of TB^{Peak} derived from daily nPDF of closed ice (SIC $>$ 98%) for V-pol (red) and H-pol (blue), using SMAP L1B TB collected north of 65°N conditioned by SIC_{NCEP} and SIC_{OSISAF}, respectively, along with the number of samples (black thin or dotted lines).

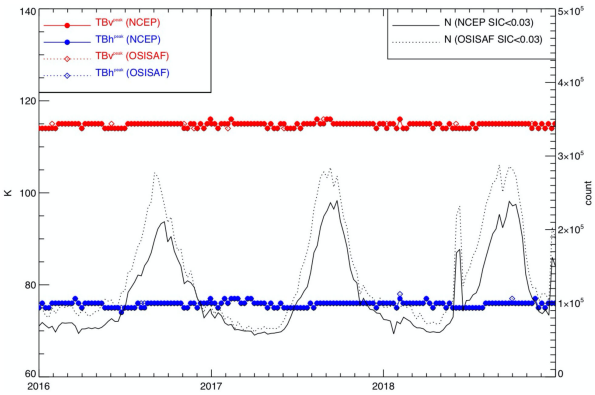

Fig. 5. Time series of TB^{Peak} derived from daily nPDF of open water (SIC $<$ 3%) for V-pol (red) and H-pol (blue), using SMAP L1B data collected north of 65°N conditioned with SIC_{NCEP} and SIC_{OSISAF}, respectively, along with the number of samples (black thin and dotted lines).

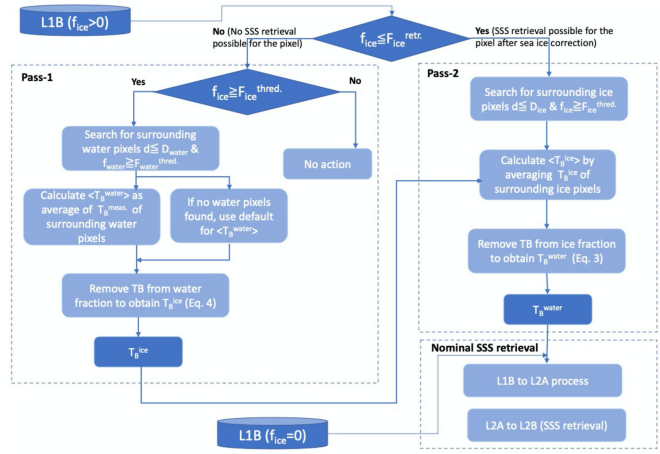

Fig. 6. Flowchart of the sea IC algorithm.

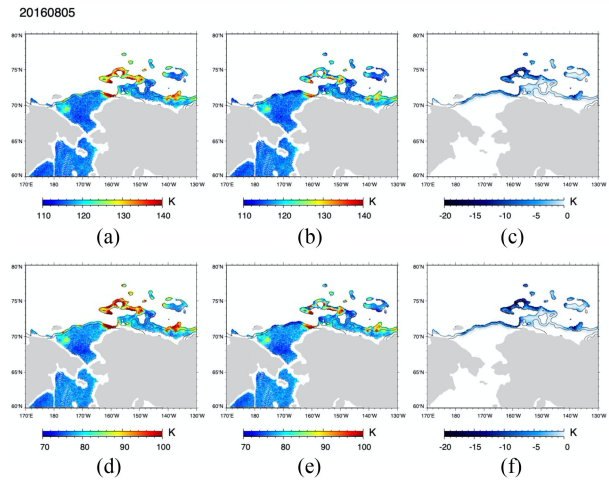

Fig. 7. SMAP L1B TBv (top) and TBh (bottom) on August 5, 2016 before (left) & after (middle) the sea IC (using $D_{\mathrm{ice}} = 2$), and the correction terms (right). Areas with ice fraction greater than 0.15 are masked out (white). Thin line (black) are the SIC contours at 3% and 15%.

coastal areas, for example, columnar water vapor content in the Baltic Sea [24], SIC [25], and wet path delay [26]. Recently, Chaubell et al. [27] adopted the SPC method for SMAP soil moisture retrieval, considering its benefit of keeping original data resolution and latency of operational processing. In this study, we develop a method similar to SCP for sea IC.

The rest of this article is organized as follows. Section II describes the data used. Section III presents an analysis of sea ice signature in SMAP L-band radiometer measurement. Section IV describes the sea IC algorithm. Section V shows the impact of IC on real data collected by SMAP. Corrected TB are used to retrieve SSS in the Arctic Ocean and compared with parallel retrieval without IC, with results presented in Section VI. In Section VII, we present results of validation comparing SMAP Level 3 daily SSS with in situ salinity data collected around the coast of Greenland in NASA's Ocean Melting Greenland (OMG) mission. Finally, a discussion and conclusions will be given in Section VIII.

II. Data

A. Brightness Temperature

We use the newly released SMAP Version 5 (V5) Level-1B (L1B) TB to characterize the effect of sea ice on L-band radiometer and develop an empirical correction algorithm. SMAP L1B TB data is half-orbit (ascending/descending separated), time-ordered, geolocated, calibrated in reference to the Earth's surface with undesired and erroneous radiometric sources removed [28]. SMAP's conical scanning L-band radiometer projects a ∼1000 km wide swath on earth's surface from 86.4°S to 86.4°N with 3-dB beamwidth less than 40 km and achieves a global coverage in ∼3-days with exact orbit repeat cycle of 8 days. The coverage in high latitudes is even better with most areas poleward of 60° being covered in one day. L1B V5 TB data from March 31, 2015, to be presented are available from the National Snow and Ice Data Center (NSIDC).[1]

[1][Online]. Available: https://nsidc.org/data/SPL1BTB

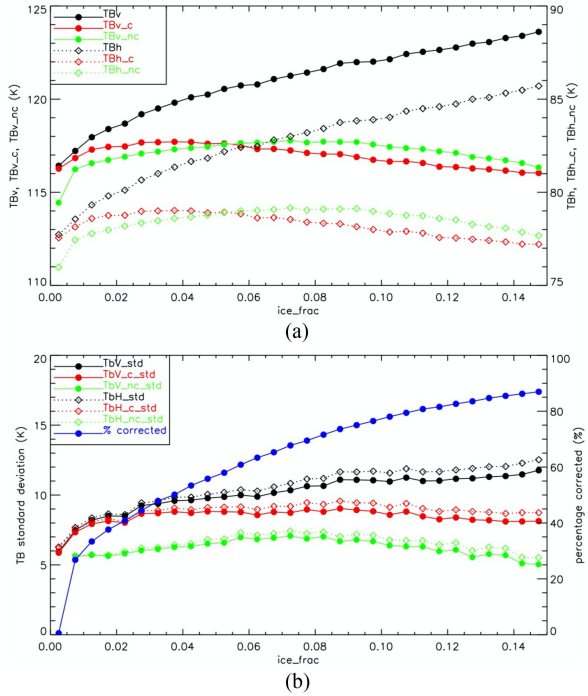

Fig. 8. SMAP L1B brightness temperature (TB) bin-averaged as function of sea ice fraction. (a) TB before (black, TBv and TBh) and after (red, TBv_c and TBh_c) the sea IC, and TB measured in footprints where ice fraction is non-zero but no IC was performed (green, TbV_nc and TbH_nc). (b) Standard deviation corresponding to each set shown in (a), and blue curve is the percentage of L1B pixels where sea IC performed. All are based on 4 months of data collected north of 50°N from June. 1 to Sep. 30, 2016.

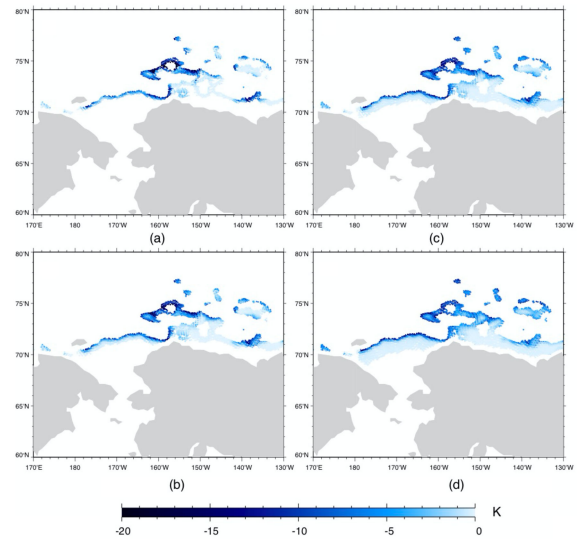

Fig. 9. Sea IC of SMAP L1B dTBv (TB_corrected minus measured) using ice sea radius of (a) $D_{\rm ice} = 1$, (b) $D_{\rm ice} = 2$, (c) $D_{\rm ice} = 3$, and (d) $D_{\rm ice} = 5$ on August 5, 2016, in the Beaufort Sea, excluding areas with ice fraction greater than 0.15 (white).

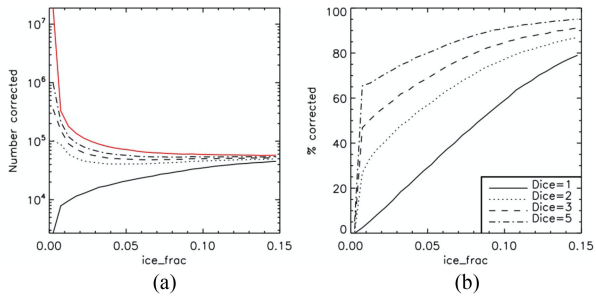

Fig. 10. (a) Applying the sea IC on SMAP L1B data north of 50°N from June 1 to Sep. 30, 2016, number L1B pixels corrected using $D_{\rm ice}$ of 1 (solid line), 2 (dotted line), 3 (dashed line), and 5 (dot-dash line), and the red curve indicates the total number of L1B pixels with ice_frac >0.0. (b) Percentage of L1B pixels where sea IC performed.

B. SMAP Sea Surface Salinity

The combined active-passive (CAP) retrieval algorithm originally developed at JPL in the context of Aquarius/SAC-D [29] is adopted for SMAP SSS retrieval [15]. The standard JPL SSS data are provided on both Level 2B (L2B) and Level 3 (L3) [16]. The L2B data are on a 25-km grid along/cross track of ∼1000 km wide swath (∼15 swaths per day) with an effective spatial resolution of 60 km (see [15] for L1B to L2B CAP processing). The L3 data is on global map grid with 0.25° resolution in latitude and longitude. We use Gaussian weighting to interpolate the L2B estimates onto the map grid with a search radius of ∼ 45 km and a half-power radius of 30 km. L3 maps are produced both monthly and daily which is the 8-day running mean of L2B data centered on the day. JPL SSS data are publicly available from April 1, 2015, to present with a 3-day latency in processing and availability at PO.DAAC.[2]

In this study, we use the JPL CAP software to retrieve L2B SSS with or without IC. For L3 daily maps, we reduce the temporal window to 4 days to take advantage of more frequent polar satellite coverage. This better captures SSS variation near the sea ice edge. We also use, as a reference, the ancillary SSS from Global Ocean Prediction with the HYbrid Coordinate Ocean Model (HYCOM) [30], which is routinely matched up with SMAP measurements based on source file download from FTP.OPC.NCEP website.[3] and included in JPL L2B and L3 SSS products.

C. Sea Ice Concentration

Since SIC data have large uncertainty near the ice edge, especially in summer (∼ 5–15%; [31]), we examined two sets of SIC data. The first is produced by the National Centers for Environmental Prediction (NCEP) of NOAA ($\rm SIC_{NCEP}$), which is available daily on a 1/12° grid.[4] The second is from the Ocean and Sea Ice Satellite Application Facility (OSISAF) of the European operational satellite agency EUMETSAT ($\rm SIC_{OSISAF}$). $\rm SIC_{OSISAF}$ is computed from atmospherically corrected SSMIS brightness temperatures using a combination of algorithms ([32] and references therein). $\rm SIC_{OSISAF}$ is produced daily with global coverage and spatial sampling of 10 km and is available at OSI

[2][Online]. Available: https://podaac.jpl.nasa.gov/dataset

[3][Online]. Available: http://ftp.opc.ncep.noaa.gov/grids/operational/GLOBALHYCOM/Navy

[4][Online]. Available: https://polar.ncep.noaa.gov/seaice/index.html

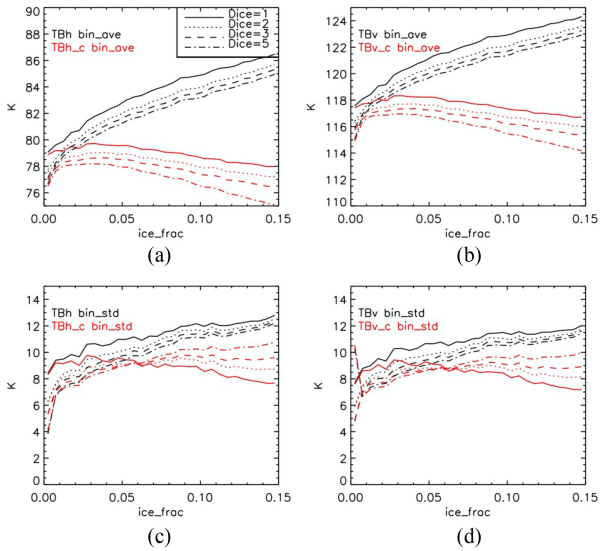

Fig. 11. Similar as Fig. 8 for various D_{ice}, bin-averaged (a) TBh, (b) TBv, and bin-standard-deviation for (c) TBh, (d) TBv before (black) and after (red) the sea IC.

SAF website.[5] Both SIC data sets are collocated with the centers of SMAP L1B footprint (nearest neighbor).

D. Sea Ice Fraction

Sea ice fraction (f_{ice}) is the fraction of the radiometer footprint, or field of view (FOV), covered by sea ice. f_{ice} is estimated via the integration below [33]

$$f_{\text{ice}}(x,y) = \int_{FOV} \text{SIC}(x,y)\, G(\theta,\varphi)\, d\Omega / \int_{FOV} G(\theta,\varphi)\, d\Omega \tag{1}$$

where G is the SMAP antenna total gain pattern (sum of copolarization and cross-polarization gains), SIC(x, y) is interpolated to antenna sampling location on earth surface location (x, y), and $d\Omega$ is the solid angle of the integration. We used SIC_{NCEP} to calculate f_{ice} on each SMAP L1B pixel.

E. Salinity From AXCTD/OMG

SMAP SSS retrievals are validated with in-situ salinity collected by the NASA mission OMG [34], [35]. The goal of OMG is to understand the role that the ocean plays in melting Greenland's glaciers. From 2016 to 2020, OMG conducted field campaigns to gather ocean data around Greenland. One component of OMG measurements is an annual summertime aircraft campaign that deploys along the continental shelf ~250 Airborne eXpendable Conductivity Temperature Depth (AXCTD) instruments. These instruments are launched from an aircraft, fall under a small parachute, and float on the surface after impact. The floating portion then releases a probe, which sinks to the bottom or a depth of 1000 m, whichever is shallower. The probe is connected to the surface float by a thin wire, which unspools as the probe sinks, measuring temperature and conductivity as a function of time, which can be converted to temperature and salinity as a function of depth. We acquired OGM AXCTD data from PO.DAAC at[6] [36].

III. Characteristics of L-Band Sea Ice Signature

We show as an example the vertically and horizontally polarized TB (TBv and TBh) and the difference (dTB = TBv-TBh), along with SIC_{NCEP}, on two typical days: April 22, 2016, which represents the beginning of the sea ice melt season (see Fig. 1), and on August 26, 2016 (see Fig. 2) near the end of summer ice melt. SIC contours overplotted on each map indicate four values: 3% is the upper limit of current SSS retrieval, 15–30% represent the Marginal Ice Zone (MIZ), and 98% represents closed ice. TBv, TBh, and dTB all show large spatial gradients in the MIZ.

We divided SMAP TBs collected north of 65°N into four categories according to matchup SIC:

1) Open water (SIC $<$ 3%).
2) Ice edge with less ice (3–15%).
3) More ice (15–30%).
4) Closed ice (SIC $>$ 98%).

We defined a normalized distribution of TB (nPDF) in each category conditioned by SIC_{NCEP} and $\text{SIC}_{\text{OSISAF}}$ by dividing the number collected in each TB bin (bin size of 1K) by the total number of TBs in the category. Fig. 3 shows nPDF on the two days shown in Figs. 1 and 2. Through the ice melt season, the population of the closed ice category on a typical day (blue curves in Fig. 3) dropped from near 280 (233) thousand to less than 8 (7) thousand based on SIC_{NCEP} ($\text{SIC}_{\text{OSISAF}}$). The most interesting feature shown in Fig. 3 is that peaks of nPDF in the ice edge categories (red and green curves) well agree with the peak of open water (black). This is an indication that a large part of measurements collected in the ice edge contain useful information for SSS retrieval. As expected, the tails of nPDF of the two ice edge categories extend towards higher TB values, with larger spread in category 3 (more ice). Fig. 3 also confirms the polarization difference dTB (i.e., the horizontal difference between peaks of solid and dashed curves) is much smaller for closed ice than other categories. The difference in nPDFs derived based on different SIC products is an indication of large uncertainty in SIC.

Fig. 4 shows the time series of peak TB for the closed ice category (SIC $>$ 98%) based on the daily nPDF produced using SMAP data from 2016 to 2018. We found in the two-month period following the onset of sea ice melt (which usually happens in late April or early May), TB over ice drops more than 30K, likely caused by surface condition changes associated with snow cover, melting ponds, or seasonal warming of the ice surface [37]. On the other hand, TB peaks derived for the open water category (SIC $<$ 3%) are quite stable over time (see Fig. 5).

IV. Sea IC Algorithm

A. Description of the Approach

We propose a data-driven approach to extract emission from the water portion of measured TB collected in scenes with mixed

[5][Online]. Available: http://www.osi-saf.org/?q=content/global-sea-ice-concentration-ssmis

[6][Online]. Available: https://podaac.jpl.nasa.gov/dataset/OMG_L2_AXCTD

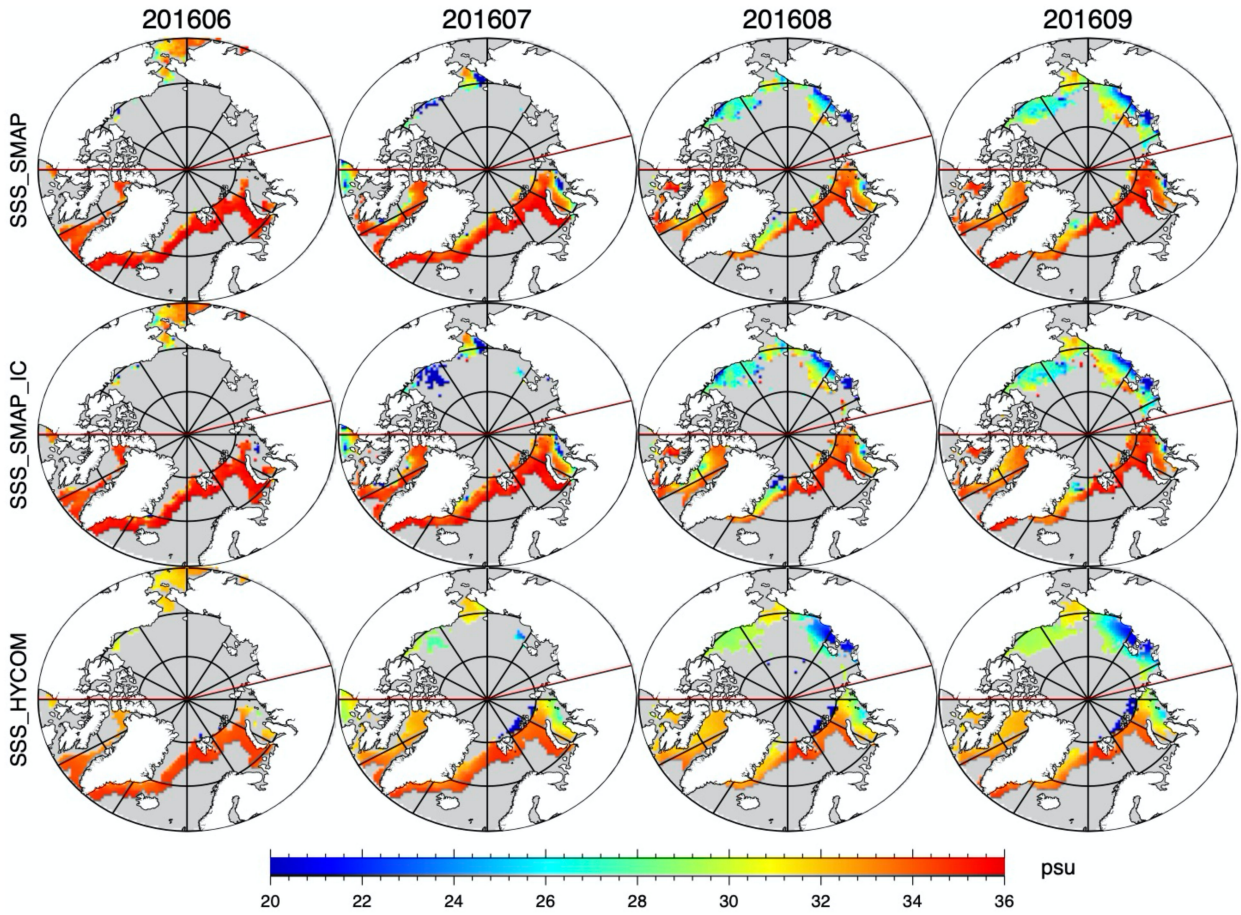

Fig. 12. Monthly average of SSS retrieved in area with SIC greater than zero, (top) without sea IC, (middle) with sea IC, and (bottom) HYCOM SSS from June to Sep. 2016 (left to right). Red line indicates the division of Arctic ocean adjacent to Pacific and Atlantic.

water and ice. Emission of the ice portion of the footprint is removed based on estimation according to the ice fraction (f_{ice}) in the satellite footprint and using the ice signature derived from surrounding pixels. We first specify a threshold of sea ice fraction, $F_{ice}^{retr.}$, as the maximum ice fraction of an L1B TB pixel on which the sea IC is applied before SSS retrieval. In this study, we use $F_{ice}^{retr.} = 0.15$, which is the traditional definition of the ice edge in terms of SIC [38]–[40]. Note that although f_{ice} and SIC are two different parameters (1), their large-scale spatial patterns are similar. We consider the choice of $F_{ice}^{retr.} = 0.15$ as equivalent to attempting to retrieve more SMAP SSS data closer to the ice edge relative to existing algorithms.

Under the assumption that in a satellite FOV mixed with sea ice and water, radiometer measured TB ($TB^{meas.}$) represents the sum of emission from ice and water portion, which is proportional to f_{ice} and f_{water} respectively, we have,

$$TB^{meas.} = (1 - f_{ice})\ TB^{water} + f_{ice} TB^{ice} \quad (2)$$

where the two unknowns, TB^{ice} and TB^{water}, are assumed to be constant over their respective portion within the FOV under consideration.

Our proposed approach is to obtain an estimation of TB^{ice} and TB^{water} for each pixel using SMAP measurements in the adjacent area surrounding the pixel under consideration. Specifically, for a given L1B pixel (i, j) with $0\% < f_{ice} < 15\%$, we substitute TB^{ice} in (2) with a representative $<TB_{i,j}^{ice}>$ derived from pixels surrounding (i, j). Rearranging (2) we have TB^{water} at pixel (i, j) as

$$TB^{water}(i,j) = \frac{TB^{meas.}(i,j) - f_{ice}(i,j)\left\langle TB_{i,j}^{ice}\right\rangle}{1 - f_{ice}(i,j)}. \quad (3)$$

Then TB^{water} can be used as input into CAP SSS retrieval routines designed for sea water. The key element here is to find $<TB_{i,j}{}^{ice}>$ that optimally represents the emissivity from the ice portion of footprint (i, j), which we describe in detail next in Section IV-B.

B. Estimation of the Ice Surface Brightness Temperature

To determine $<TB_{i,j}^{ice}>$ in (3), we extract information from TB measured over "ice" pixels surrounding (i, j). "Ice" here is in quotation marks because these pixels might not be 100% ice. The design of the algorithm is based on consideration of two issues regarding the selection of "ice" pixels: 1) what is an appropriate criterion for an "ice" pixel? 2) how far from (i, j) should we search for those "ice" pixels?

Previous studies on the application of radiometer data near the coast used a very high-resolution land mask to separate pixels

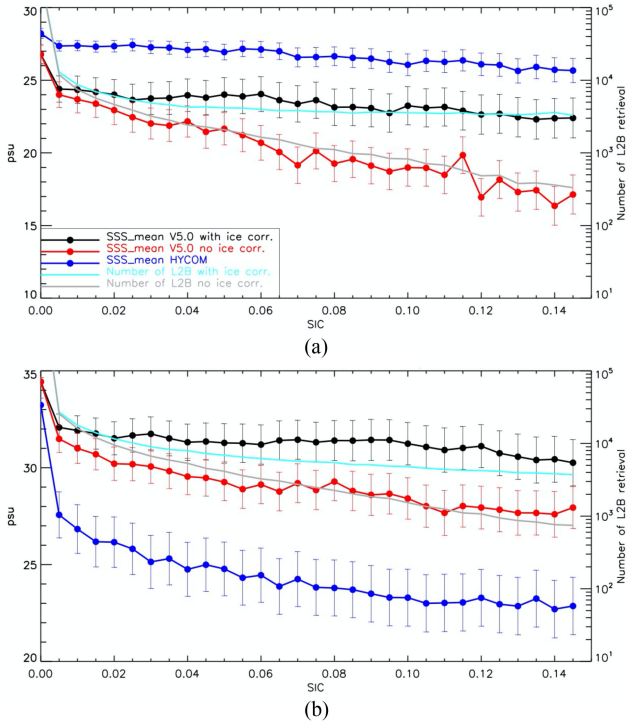

Fig. 13. SMAP L2B SSS as function of SIC with (black) or without (red) sea IC, and from HYCOM matchups (blue). All derived from four months (June to Sep. 2016) of data north of 65°N, averaged in Arctic region (a) adjacent to northern Pacific including the Beaufort Sea, Chukchi Sea, East Siberian Sea, and Laptev Sea (90°W to 105°E), and (b) adjacent to Northern Atlantic including Kara sea, Barents sea, Greenland sea, and Baffin Bay (105°E to 90°W). Vertical lines indicate means ±10% of the standard deviation.

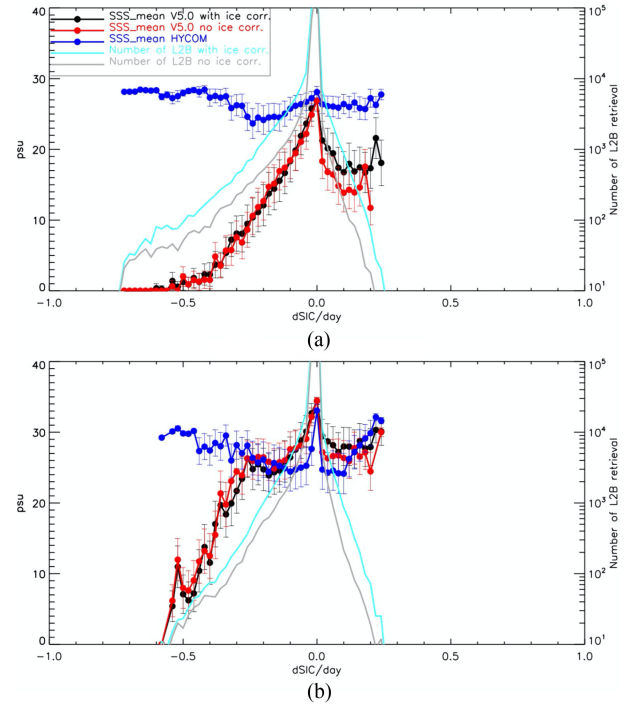

Fig. 14. Similar as Fig. 13, SMAP L2B SSS as function of sea ice change (dSIC/dt).

over land and water in terms of the center locations of the satellite footprints [24], [27]. Considering the dynamical nature of sea ice and the large uncertainty in SIC products, we decided to use $f_{\rm ice}$ to distinguish ice and water pixels. For a given threshold $F_{\rm ice}^{\rm thred.}$, pixels with $f_{\rm ice}$ greater than $F_{\rm ice}^{\rm thred.}$ are considered as "ice." The possible choice of $F_{\rm ice}^{\rm thred.}$ ranges from $F_{\rm ice}^{\rm retr.}$ to 1. Choosing the low bound ($F_{\rm ice}^{\rm thred.} = F_{\rm ice}^{\rm retr.}$) implies some of the pixels selected as "ice" could have very similar conditions to the pixel (i, j) under consideration, such as surface roughness, melt ponds, snow cover, ice age (first year or multiyear ice), ice pack state (closed or open), etc. On the other hand, the upper bound of $F_{\rm ice} = 1$ means that only pixels with 100% ice are selected. While this might appear desirable, in fact, the surface conditions of closed ice may be very different from the condition at the ice edge where pixel (i, j) is located. Because our purpose is to find an optimal representative $T_{\rm B}^{\rm ice}$ for pixel (i, j), we decided to use $F_{\rm ice}^{\rm thred.} = F_{\rm ice}^{\rm retr.}$. This choice also allows more freedom in dealing with the second issue, i.e., selecting an appropriate area over which to search for "ice" pixels surrounding (i, j). A too-small searching area could result in no adjacent pixels meeting the "ice" criterion, while a too-large area may not represent the condition at (i, j). We conducted a series of experiments using various searching radii ($D_{\rm ice}$), from 1 grid space on L1B swath (i.e., only considering the adjacent nearest neighbors of (i, j)) to $D_{\rm ice}$ of 2, 3, and 5 grid spaces.

The next step is to remove the emission from the water portion of the footprints identified as "ice". Particularly for those pixels with $f_{\rm ice}$ very close to $F_{\rm ice}^{\rm thred.}$, the water contribution to $T_{\rm B}^{\rm meas.}$ may not be ignored. The concept described above can be applied here, by reversing the places of ice and water. Specifically, for each "ice" pixel (i_0, j_0), we have,

$$T_B^{\rm ice}(i_0, j_0) = \frac{T_B^{\rm meas.}(i_0, j_0) - (1 - f_{\rm ice}(i_0, j_0))\left\langle T_{B,i_0,j_0}^{\rm water}\right\rangle}{f_{\rm ice}(i_0, j_0)} \tag{4}$$

where $<T_{i_0,j_0}^{\rm water}>$ is an average of measured TB over "water" pixels surrounding (i_0, j_0). Since the variation over water is much smaller than over ice, we used $D_{\rm water} = 20$ grid spaces to select a set of near homogeneous "water" pixels ($f_{\rm ice}$<0.005).

Finally, we obtain $<{\rm TB}_{i.j}^{\rm ice}>$ as the average of ${\rm TB}_{i0.j0}{}^{\rm ice}$ over $N_{i,j}$ ice pixels surrounding (i, j). If no "ice" pixel was found surrounding (i, j), no sea IC is performed even if $f_{\rm ice}$ is nonzero.

C. Two-Pass Scheme and Quality Control

The concept described above is implemented in a two-pass correction scheme and summarized in Fig. 6. With the selection of $F_{\rm ice}^{\rm thred.} = F_{\rm ice}^{\rm retr.}$, the L1B measurements collected in one satellite orbit are divided into two sets: the "ice" set ($f_{\rm ice} > F_{\rm ice}^{\rm retr.}$), and the "water" set ($f_{\rm ice} < F_{\rm ice}^{\rm retr.}$). In the first pass, the process removes the emission from the water portion of each footprint in the "ice" set to obtain ${\rm TB}^{\rm ice}$ (4). In the second pass, ${\rm TB}^{\rm ice}$ obtained in pass-1 are used to calculate ${\rm TB}^{\rm water}$ for each pixel (i, j) with $f_{\rm ice} < F_{\rm ice}^{\rm retr.}$ (3). Additional quality controls are implemented to eliminate unrealistic corrections, which includes (1) in pass-1 for ice pixel if $<{\rm TB}^{\rm water}>$ derived from surrounding water pixels exceeds ${\rm TB}^{\rm meas.}$; and (2) in pass-2, for water pixel

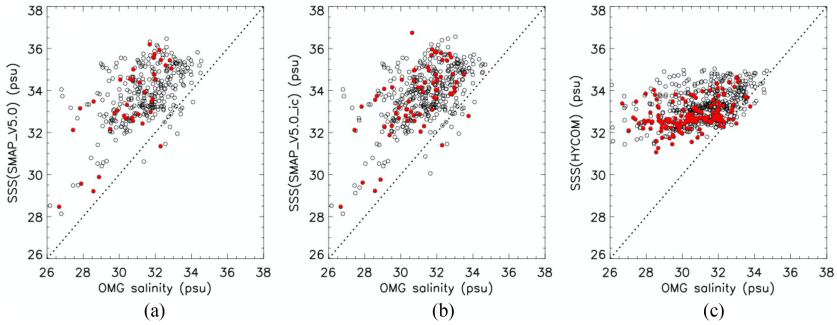

Fig. 15. Scatterplot of collocated SSS_{OMG} and Level 3 (a) SSS_{SMAP} (no sea IC), (b) $SSS_{SMAP\cdot IC}$ (with sea IC) and (c) SSS_{HYCOM} (nearest neighbor). Black open circles are for total matchups, and red dots for where there is sea ice (SIC>0.0). The dotted line is the 1:1 as a reference.

if $<TB^{ice}>$ derived from surrounding ice pixels is less than $TB^{meas.}$.

V. Impact of Sea IC on TB

We applied the algorithm described above to SMAP L1B TB data. We first present the results of the correction using $D_{ice} = 2$. Fig. 7 shows, as an example, SMAP TBs with or without IC in the Beaufort Sea on August 5, 2016. Areas within ~35 km of the coast and with ice fraction larger than 0.15 (where no IC was attempted) are masked in white in panels (a), (b), (d), and (e) for easier visualization. Before the correction [see Fig. 7(a) and (d)] pixels with high TB were observed in the northern edge of the domain (reddish color), which obviously contained emission from ice. After applying IC, TB_ic [see Fig. 7(b) and (e)] were reduced into a reasonable range for seawater (bluish color). The map of the correction term, i.e., dTB = TB_ic – TB, [see Fig. 7(c) and (f) where white color indicates no correction] show that IC indeed took place in an inhomogeneous area between solid ice in the north and open water in the south. Generally speaking, larger corrections (dark blue color) occurred in the northern edge of the domain close to packed ice, while smaller corrections (light blue color) occurred in the southern edge close to open water. White patches embedded in the dTB maps were places where ice fraction exceeded the upper limit of the correction algorithm.

For a broader assessment of the impact of sea IC on SMAP TB, we analyzed four months of data for the ice melting season in the northern hemisphere from June to September of 2016. We bin all data north of 50°N in terms of ice fraction with a bin size of 0.005. We discuss the result (see Fig. 8) from three aspects. First, we found that the trend of $TB^{meas.}$ (uncorrected) increasing with f_{ice} (black) was effectively flattened in TB_ic (red), and the standard deviation significantly decreased. Second, the IC reduction in TBs for H-pol [see Fig. 8(a), right axis] is slightly larger than that for V-pol (left axis), reaching maximum of 9K and 8K respectively at ice fraction threshold of 0.15. This is consistent with the fact that the L-band TB difference between ice and water for H-pol is larger than V-pol therefore H-pol is expected to be more sensitive to the IC. Last, we point out that the IC algorithm seems most effective for f_{ice} close to the upper limit, $F_{ice}^{thred.}$. The percentage of corrected-TB [see Fig. 8(b), blue curve] was close to 90% at f_{ice} of 0.15, while less than 30% at f_{ice} of 0.01. This is because the algorithm takes no action at places where no adjacent ice pixel is found. Fig. 8 (green) shows that the bin-average and std. of TB for those "no-correction" pixels (i.e., $f_{ice}>0$ but dTB = 0) are in the reasonable range of seawater and almost "flat" versus f_{ice}. We argue that this indicates that no correction is needed in the algorithm design in these areas.

We examined the sensitivity of IC on the choices of D_{ice} (ice searching radius) by repeating IC using a series of D_{ice} values (1, 2, 3, and 5 grid spaces of L1B swath). This is equivalent to extracting TB^{ice} in a surrounding area of size from 40×40 km^2 (for $D_{ice} = 1$) to 200×200 km^2 (for $D_{ice} = 5$). Fig. 9 shows the correction term dTB in the Beaufort Sea on Aug. 5, 2016, for V-pol, as an example. It is clear that a larger D_{ice} leads to the expansion of area covered by IC southward towards open water, where the chance of finding adjacent ice pixels increased. The sensitivity on D_{ice} is shown as a function of f_{ice} as the number (or percentage) of SMAP L1B pixels corrected by the IC algorithm (see Fig. 10), and also as the bin-average and std of TB with or without IC (see Fig. 11). Although the percentage of corrected measurements monotonically increases with D_{ice} for a given ice fraction (see Fig. 10), the problem of over-correction becomes more severe with large D_{ice}. For example, IC with $D_{ice} = 5$ resulted in a reduction of more than 3K from f_{ice} near zero to 0.15 [see Fig. 11(a) and (b)]. On the other hand, the sensitivity of bin-std [see Fig. 11(c) and (d)] on D_{ice} shows two different regimes with a transition at f_{ice} around 0.05: with std. decreasing with D_{ice} for small f_{ice} regime while increasing with D_{ice} for the larger f_{ice} regime. This seems to suggest that the IC algorithm may benefit from a hybrid of D_{ice} values. We leave this for future study.

In terms of the impact of IC on TB, we conclude that using an ice search radius D_{ice} of 2 in pass-2 provides an optimal solution, covering the most critical area near the ice edge and avoiding the possibility of severe over-correction.

VI. SMAP SSS in Arctic Seas

Fig. 12 compares the 2016 monthly averaged SSS in the Arctic Seas (north of 65°N) from three datasets: SMAP SSS without IC (top), SMAP SSS with IC (middle), and SSS from HYCOM. All three SSS fields (named SSS, $SSS_{IC,}$ and SSS_{HYCOM} hereafter)

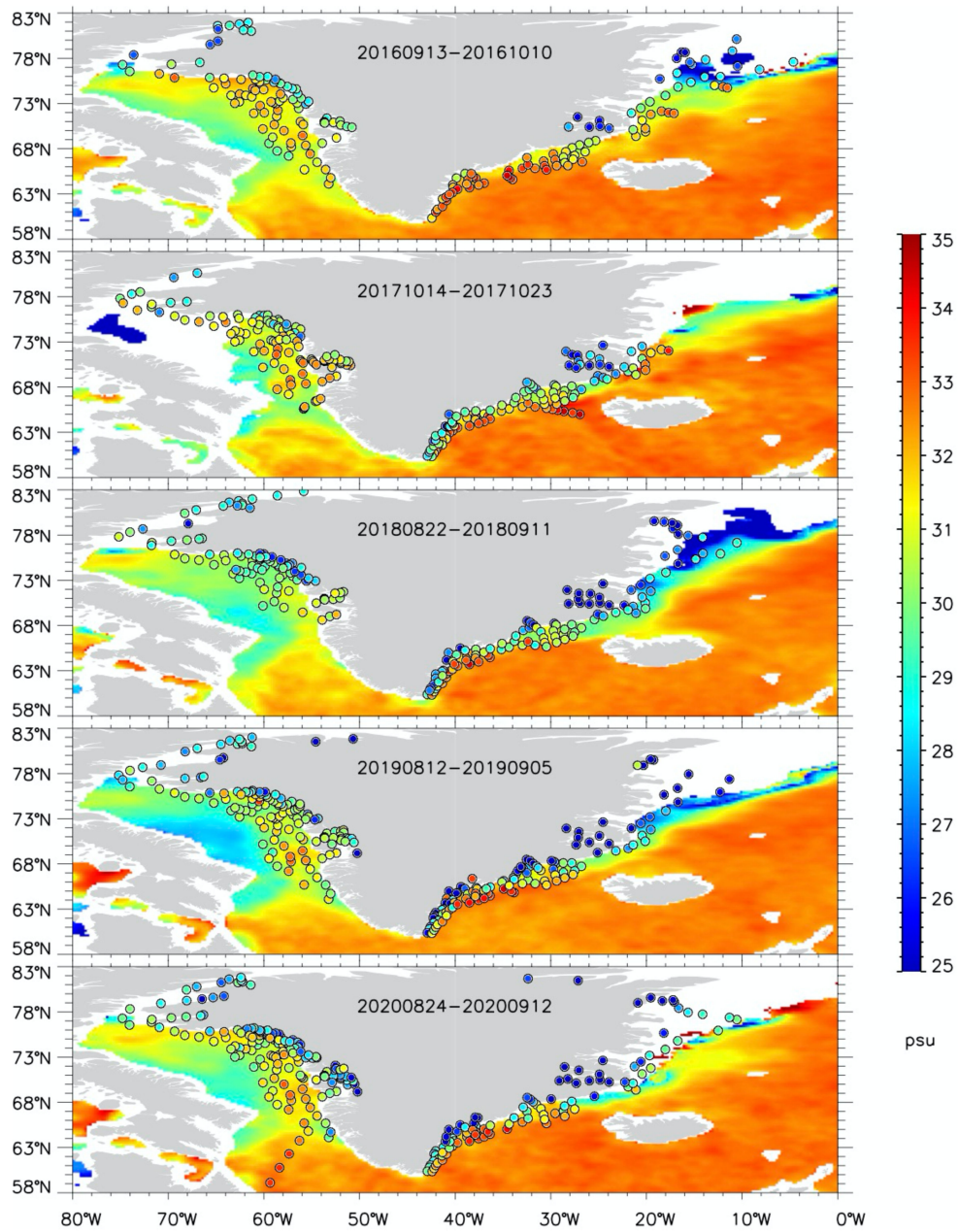

Fig. 16. SMAP SSS (with sea IC) maps averaged over the period of OMG campaign for each year from 2016 to 2020 (background color), and solid dots are OMG/AXCTD salinity at depth of 0.72 m from surface.

show a similar large-scale pattern: saltier in the northern Atlantic Ocean and fresher in the marginal seas connected to the Pacific Ocean through Bering Strait. Generally speaking, SMAP SSS shows more intra-seasonal variability than HYCOM, from the onset of the melting season in June to the beginning of the freezing phase in September. In particular, freshening in the Beaufort Sea associated with seasonal ice melting and river discharge observed by SMAP is completely missed in HYCOM. This model deficiency might arise from a number of reasons, e.g., climatological surface salinity restoring, virtual salt flux boundary conditions, overly large mixing rates, etc. We have masked out areas where SIC is zero or larger than 0.15 (where no IC is applied) in Fig. 12 for the convenience of visualization. Although it is hard to visualize the impact of IC in the monthly averaged maps, we can identify several areas where SSS_{IC} provides slightly more retrieval, for example, in the Beaufort Sea (July and August), the Chukchi Sea (August), and the Greenland Sea (August). Both SSS and SSS_{IC} increase north of the East Siberian Sea in September when freezing starts. There is also a zonal band of low SSS just north of the Barents Sea in HYCOM that is not evident in the satellite data.

To compare the three products quantitatively, we divided the Arctic Ocean into two domains, Arctic_Pacific and Arctic_Atlantic (divided at longitude 90°W and 105°E, indicated by the red lines in Fig. 12). Fig. 13 shows the bin-averaged SSS versus SIC based on L2B data north of 65°N from June to

Sep. of 2016. Here we used SIC matching with L2B grid since the information of $f_{\rm ice}$ is only available for L1B footprint. SSS retrieved from SMAP TB with IC (SSS_{IC}, black curve) is higher than SSS without IC (SSS, red curve) by more than 5 psu at the upper limit of SSS retrieval (SIC $\sim$0.15). The dependence on SIC is almost removed in SSS_{IC}. On the other hand, bin-averaged HYCOM SSS (blue curves) in Arctic_Pacific ($\sim$27 psu) is higher than in Arctic_Atlantic ($<$ 25 psu), which is likely a result of the fresh SSS band north of the Barents Sea (see Fig. 12).

Fig. 14 shows the same three SSS datasets binned as a function of sea ice changes, i.e., the time derivative of SIC (dSIC/dt). It is interesting to see the asymmetric distribution of SSS between melting phase (dSIC/dt$<$0) and freezing phase (dSIC/dt$>$0). In the melting phase, SMAP SSS decreases with the increasing speed of ice melting, which agrees with the intuition that more rapid ice melting should inject more low-SSS meltwater into adjacent seawater. This is similar to the cold SSTs seen in the wake of retreating sea ice [38]. HYCOM SSS, however, is relatively insensitive to the magnitude of negative dSIC/dt. There seems no significant difference between SMAP SSS with or without IC in the melting phase. In the freezing phase, SSS is not as sensitive to dSIC/dt. SMAP SSS with IC is generally higher than SSS without IC, although this difference is not statistically significant. The difference likely arises from retrieval differences in the ice front as seen in Fig. 12. We note that in the Arctic_Atlantic, SMAP SSS and HYCOM behave similarly, i.e., a decline for dSIC/dt $>$ 0.1/day, then an increase with dSIC/dt.

VII. Validation With OMG Data

In the last two sections, we analyzed the impact of sea IC on TB and retrieved SSS. A systematic validation is a challenge due to lack of in situ SSS measurements in the challenging Arctic environment, particularly near the ice edge. Here we present a validation using OMG AXCTD data along the coast of Greenland.

Data returned by the OMG aircraft campaign covered slightly different time periods in each year: Sep.13 to Oct. 10, 2016 (184 profiles); Oct. 14 to Oct. 23, 2017 (217 profiles); Aug. 12 to Sep. 11, 2018 (216 profiles), Aug. 12 to Sep. 5, 2019 (261 profiles), and Aug. 24 to Sep. 12, 2020 (262 profiles). There are a total of 1140 AXCTD temperature/salinity profiles with OMG data quality control. We use AXCTD salinity measured at a depth closest to surface (i.e., $\sim$0.72 m, denoted as SSS_{OMG}).

For each OMG/AXCTD probe, we created SMAP matchups from gridded daily (4 days running mean) from the nearest-neighbors with valid SSS, which was closest in distance to OMG location. Data pairs where matchup SIC is larger than 0.15 are excluded. We also used the SMAP SSS uncertainty (which is reported as a measure of retrieval error in JPL SMAP products) to exclude points of possible bad retrieval due to undetected ice/land contamination or other measurement errors (L3 SMAP_SSS_uncertainty $>$ 1 psu).

The comparison of the matchups for each set of SSS_{SMAP}, $SSS_{MAP\text{-}IC}$, and SSS_{HYCOM} versus SSS_{OMG} are presented in Fig. 15 and Table I. The number of pairs collocated with OMG increased from 329 pairs without sea IC to 432 pairs with sea IC,

TABLE I
Comparison of SSS_{OMG} and Collocated SSS_{SMAP} (No Sea IC), $SSS_{SMAP\text{-}IC}$ (With Sea IC) and SSS_{HYCOM}

	X	Number of matchups	Mean of difference	Std. of difference
All matchups	SMAP	329	2.44	1.42
	SMAP_IC	432	2.47	1.41
	HYCOM	616	2.23	1.53
SIC>0	SMAP	37	2.72	1.32
	SMAP_IC	67	2.66	1.40
	HYCOM	170	2.38	1.52

Note difference is X minus SSS_{OMG}.

an increase of more than 30%. Both SSS_{SMAP} and $SSS_{SMAP\text{-}IC}$ show a positive bias $\sim$ 2.5 psu and standard deviation around 1.4 psu. This indicates that while the proposed sea IC algorithm did not reduce errors in bias or standard deviation, it did deliver more salinity retrievals without noticeable performance degradation. As shown in Fig. 16, $SMAP_{SSS\text{-}IC}$ (adjusted by subtracting 2.5 psu bias) shows good agreement with the salinity pattern revealed by SSS_{OMG}. We see that SMAP not only depicted the large contrast between the east and west coasts of Greenland consistent with OMG but also captured small scale salinity features as well as the sharp salinity gradient away from the coast. The fresh area observed in 2018 northwest of Greenland is likely a sampling of the relatively fresh East Greenland Current outflow from the Arctic Ocean, possibly enhanced by Greenland glacial melt.

VIII. Discussion and Conclusion

We presented a data-driven algorithm to improve SSS retrieval near the ice edge. The method extracts the signal received from the water portion of radiometer FOV by removing the contribution from the ice portion, which is derived from adjacent measurements where ice dominates. Such ice-corrected TB (i.e., TB_ic) can then be used to retrieve SSS from the JPL SMAP CAP processing system. We showed that the systematic dependence of measured TB on ice fraction (up to $f_{\rm ice} = 0.15$) was effectively removed in TB_ic. The proposed algorithm is most effective in areas near the ice edge (SIC approaching 15%) where the sea ice effect of about 90% of affected TB pixels was mitigated based on an ice signal extracted from an area $\sim$80 $\times$ 80 km^2 (Dice = 2) surrounding the pixel.

We retrieved SMAP SSS for the northern hemisphere ice melting season to assess the impact of the sea IC. Comparison of SSS retrieved from SMAP TBs with or without sea IC showed about 5 psu should be attributed to ice contamination when SIC approaches 15%. SMAP SSS shows an expected response to ice melting (dSIC/dt$<$0) or freezing (dSIC/dt).

The validation using AXCTD data collected during NASA's OMG field campaigns around the coast of Greenland over five years shows that the number of SMAP L3 daily salinity retrievals in this critical region increased by more than 30% with sea IC with a comparable performance with or without IC. With a 2.5 psu bias adjustment, SMAP SSS depicts salinity patterns around Greenland consistent with OMG measurements.

It is noted that the optimal value of Dice may differ in various environments. As suggested by one reviewer, we performed validation with OMG data for SMAP SSS retrieved with IC using various ice search radius (Dice = 1, 2, 3, and 5). Here, we used SMAP L2B data instead of L3 (since L3 involves spatial/temporal averaging which may dilute the impact of Dice). The RMSD between 1321 pairs of OMG/SMAP (collocated within 25 km and 12 h) are 3.02, 2.95, 2.92, and 2.98 psu for Dice of 1, 2, 3, and 5, respectively. Although Dice 3 seems to give the best result, we consider the difference between various Dice is not statistically significant. In fact, many SSS retrieval with difference Dice have identical values. This is due to the fact that all OMG locations are close to land mass therefore a larger Dice may not be able to find more "ice" pixels to affect the IC. We expect the situation near ice edge to be very different where pixels surrounding the target pixel are mixed with ice and water.

Future improvement of proposed IC algorithm, including the development of a methodology to optimize the ice search radius, will need the guidance based on in situ data analysis particularly near ice edge under various conditions.

ACKNOWLEDGMENT

Copyright 2021 California Institute of Technology. Government sponsorship acknowledged.

REFERENCES

[1] R. Kwok, "Outflow of Arctic Ocean sea ice into the Greenland and Barents seas: 1979–2007," *J. Climate*, vol. 22, pp. 2438–2457, 2009, doi: 10.1175/2008JCLI2819.1.

[2] R. Kwok and N. Untersteiner, "The thinning of Arctic sea ice," *Phys. Today*, vol. 64, pp. 36–41, 2011, doi: 10.1063/1.3580491.

[3] S. J. Prinsenberg, "Freshwater contents and heat budgets of James bay and Hudson bay," *Continental Shelf Res.*, vol. 3, pp. 191–200, 1984.

[4] E. C. Carmack *et al.*, "Freshwater and its role in the Arctic marine system: Sources, disposition, storage, export, and physical and biogeochemical consequences in the Arctic and global oceans," *J. Geophys. Res. Biogeosci.*, vol. 121, pp. 675–717, 2016. [Online]. Available: https://doi.org/10.1002/2015JG003140

[5] W. Tang *et al.*, "The potential and challenges of using SMAP SSS to monitor Arctic ocean freshwater changes," *Remote Sens.*, vol. 10, 2018, Art. no. 869.

[6] W. Tang *et al.*, "The potential of space-based sea surface salinity on monitoring the Hudson bay freshwater cycle," *Remote Sens.*, vol. 12, 2020, Art. no. 873, doi: 10.3390/rs12050873.

[7] G. Lagerloef *et al.*, "The aquarius/Sac-D mission: Designed to meet the salinity remote-sensing challenge," *Oceanography*, vol. 21, no. 1, pp. 68–81, 2008.

[8] D. Entekhabi *et al.*, "The soil moisture active passive (SMAP) mission," *Proc. IEEE*, vol. 98, no. 5, pp. 704–716, May 2010.

[9] Y. H. Kerr *et al.*, "The SMOS mission: New tool for monitoring key elements of the global water cycle," *Proc. IEEE*, vol. 98, no. 5, pp. 666–687, 2010.

[10] J. Font et al*et al.*., "SMOS: The challenging sea surface salinity measurement from space," *Proc. IEEE*, vol. 98, no. 5, pp. 649–665, May 2010.

[11] S. Yueh, R. West, W. J. Wilson, F. Li, E. G. Njoku, and Y. Rahmat-Samii, "Error sources and feasibility for microwave remote sensing of ocean surface salinity," *IEEE Trans. Geosci. Remote Sens.*, vol. 39, no. 5, pp. 1049–1060, May 2001.

[12] S. Fournier *et al.*, "Evaluation and intercomparison of SMOS, aquarius, and SMAP sea surface salinity products in the Arctic Ocean," *Remote Sens.*, vol. 11, 2019, Art. no. 3043.

[13] N. Vinogradova *et al.*, "Satellite salinity observing system: Recent discoveries and the way forward," *Front. Mar. Sci.*, vol. 6, 2019, Art. no. 243. [Online]. Available: https://doi.org/10.3389/fmars.2019.00243

[14] N. Reul *et al.*, "Sea surface salinity estimates from spaceborne L-band radiometers: An overview of the first decade of observation (2010–2019)," *Remote Sens. Environ.*, vol. 242, 2020, Art. no. 111769. [Online]. Available: https://doi.org/10.1016/j.rse.2020.111769

[15] A. G. Fore, S. H. Yueh, W. Tang, B. W. Stiles, and A. K. Hayashi, "Combined active/passive retrievals of ocean vector wind and sea surface salinity with SMAP," *IEEE Trans. Geosci. Remote Sens.*, vol. 54, no. 12. pp. 7396–7404, 2016, doi: 10.1109/TGRS.2016.2601486.

[16] A. G. Fore, S. H. Yueh, W. Tang, and A. K. Hayashi, "SMAP salinity and wind speed data user's guide, version 5.0," 2020. [Online]. Available: https://podaac-tools.jpl.nasa.gov/drive/files/allData/smap/docs/%20JPL-CAP_V5/SMAP-SSS_JPL_V5.0_Documentation.pdf

[17] T. Meissner, F. J. Wentz, and D. M. Le Vine, "The salinity retrieval algorithms for the NASA aquarius version 5 and SMAP version 3 releases," *Remote Sens.*, vol. 10, 2018, Art. no. 25, doi: 10.3390/rs10071121.

[18] E. Olmedo *et al.*, "Seven years of SMOS sea surface salinity at high latitudes: Variability in Arctic and sub-Arctic regions," *Remote Sens.*, vol. 2018, 2018, Art. no. 10.

[19] J. Boutin *et al.*, "New SMOS sea surface salinity with reduced systematic errors and improved variability," *Remote Sens. Environ.*, vol. 214, pp. 115–134, 2018. [Online]. Available: https://doi.org/10.1016/j.rse.2018.05.022

[20] N. Kolodziejczyk, J. Boutin, J. L. Vergely, S. Marchand, N. Martin, and G. Reverdin, "Mitigation of systematic errors in SMOS sea surface salinity," *Remote Sens. Environ.*, vol. 180, pp. 164–177, 2016.

[21] A. Supply *et al.*, "New insights into SMOS sea surface salinity retrievals in the Arctic ocean," *Remote Sens. Environ.*, vol. 249, 2020, Art. no. 112027. [Online]. Available: https://doi.org/10.1016/j.rse.2020.112027

[22] P. Waldteufel, J. L. Vergely, and C. Cot, "A modified cardioid model for processing multiangular radiometric observations," *IEEE Trans. Geosci. Remote Sens.*, vol. 42, no. 5, pp. 1059–1063, May 2004.

[23] D. A. Roberts, M. Gardner, R. Church, S. Ustin, G. Scheer, and R. O. Green, "Mapping chaparral in the Santa Monica mountains using multiple endmember spectral mixture models," *Remote Sens. Environ.*, vol. 65, pp. 267−279, 1998.

[24] R. Bennartz, "On the use of SSM/I measurements in coastal regions," *J. Atmos. Ocean. Technol.*, vol. 16, no. 4, pp. 417–431, Apr. 1999.

[25] N. Maaß and L. Kaleschke, "Improving passive microwave sea ice concentration algorithms for coastal areas: Applications to the Baltic sea," *Tellus*, vol. 62A, pp. 393–410, 2010.

[26] C. Desportes, E. Obligis, and L. Eymard, "On the wet tropospheric correction for altimetry in coastal regions," *IEEE Trans. Geosci. Remote Sens.*, vol. 45, pp. 2139–2149, 2007, doi: 10.1109/TGRS.2006.888967.

[27] J. Chaubell *et al.*, "Improving brightness temperature measurements near coastal areas for SMAP," *IEEE J. Sel. Topics Appl. Earth Observ. Remote Sens.*, vol. 12, no. 11, pp. 4578-4588, Nov. 2019. doi 10.1109/JSTARS.2019.2951323.

[28] J. R. Piepmeier *et al.*, "SMAP L1B radiometer half-orbit time-ordered brightness temperatures," Version 5. [Indicate subset used]. Boulder, CO USA: NASA Nat. Snow Ice Data Center Distrib. Active Archive Center, 2020. [Online]. Available: https://doi.org/10.5067/ZHHBN1KQLI20

[29] S. H. Yueh *et al.*, "L-band passive and active microwave geophysical model functions of ocean surface winds and applications to aquarius retrieval," *IEEE Trans. Geosci. Remote Sens.,* vol. 51, no. 9, pp. 4619–4632, Sep. 2013, doi: 10.1109/TGRS.2013.2266915.

[30] E. P. Chassignet *et al.*, "U.S. GODAE: Global ocean prediction with the HYbrid coordinate ocean model (HYCOM)," *Oceanography*, vol. 22, pp. 64–75, 2009.

[31] D. J. Cavalieri, C. L. Parkinson, P. Gloersen, and H. J. Zwally, "Sea ice concentrations from Nimbus-7 SMMR and DMSP SSM/I-SSMIS passive microwave data, version 1," [Indicate subset used]. Boulder, CO, USA: NASA Nat. Snow Ice Data Center Distrib. Active Archive Center, 1996. doi: [Online]. Available: https://doi.org/10.5067/8GQ8LZQVL0VL

[32] OSISAF, *Product User Manual for OSI SAF Global Sea Ice Concentration*, 2017.

[33] E. P. Dinnat and L. Brucker, "Improved sea ice fraction characterization for L-band observations by the aquarius radiometers," *IEEE Trans. Geosci. Remote Sens.,* vol. 55, no. 3, pp. 1285–1304, Mar. 2017.

[34] J. K. Willis, E. Rignot, R. S. Nerem, and E. Lindstrom, "Introduction to the special issue on ocean-ice interaction," *Oceanography*, vol. 29, no. 4, pp. 19–21, 2016. [Online]. Available: https://doi.org/10.5670/oceanog.2016.95

[35] I. Fenty *et al.*, "Oceans melting Greenland: Early results from NASA's ocean-ice mission in Greenland," *Oceanography*, vol. 29, no. 4, pp. 72–83, 2016, [Online]. Available: https://doi.org/10.5670/oceanog.2016.100

[36] OMG, "OMG airborne eXpendable conductivity temperature depth (AXCTD) profiles," Ver. 1. PO.DAAC, CA, USA, 2020. [Online]. Available: https://dx.doi.org/10.5067/OMGEV-AXCT1
[37] A. C. Bliss and M. R. Anderson, "Snowmelt onset over Arctic sea ice from passive microwave satellite data: 1979–2012," *Cryosphere*, vol. 8, pp. 2089–2100, 2014. [Online]. Available: https://doi.org/10.5194/tc-8-2089-2014
[38] X. Pang, J. Pu, X. Zhao, Q. Ji, M. Qu, and Z. Cheng, "Comparison between AMSR2 sea ice concentration products and pseudo-ship observations of the Arctic and Antarctic sea ice edge on cloud-free days," *Remote Sens.*, vol. 10, no. 2, 2018, Art. no. 317. [Online]. Available: https://doi.org/10.3390/rs10020317
[39] H. F. Goessling, S. Tietsche, J. J. Day, E. Hawkins, and T. Jung, "Predictability of the Arctic sea ice edge," *Geophys. Res. Lett.*, vol. 43, pp. 1642–1650, 2016, doi: 10.1002/2015GL067232.
[40] M. Steele and W. Ermold, "Loitering of the retreating sea ice edge in the Arctic seas," *J. Geophys. Res. Oceans*, vol. 120, pp. 7699–7721, 2015, doi: 10.1002/2015JC011182.

Wenqing Tang received the Ph.D. degree in physics from Michigan State University, East Lansing, MI, USA, in 1987.

In October 1989, she joined the Climate, Oceans and Solid Earth Section, Jet Propulsion Laboratory (JPL), California Institute of Technology, Pasadena CA, USA. She has been working on scientific data analysis and retrieval algorithm development of satellite earth remote sensing data. She has been the Coinvestigator of many research projects, including the NASA Ocean VectorWind Science Team on SeaWinds scatterometers NSCAT and QuikSCAT, the NASA Global Precipitatio Measurement mission, and the NASA Energy and Water cycle Study, and was the Principal Investigator of the project producing global ocean surface vector wind fields and related geophysical parameters from space-based sensors under the NOAA Climate and Global Change Program Directed at Climate Change Data and Detection/Enhanced Data Sets. She joined the Aquarius postlaunch instrument calibration and validation team in 2011 and has been working on Aquarius radar/radiometer geophysical model functions and other research activities including the rain effect on roughness correction to improve sea surface salinity retrieval.

Dr. Tang is an Associate Editor of *JSTARS*.

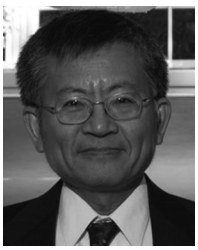

Simon H. Yueh (Fellow, IEEE) received the Ph.D. degree in electrical engineering from the Massachusetts Institute of Technology, Cambridge, MA, USA, in 1991.

From February to August 1991, he was a Postdoctoral Research Associate with the Massachusetts Institute of Technology. In September 1991, he joined the Radar Science and Engineering Section, Jet Propulsion Laboratory (JPL), California Institute of Technology, Pasadena, CA, USA. During 2002–2007, he was the Supervisor of the Radar System Engineering and Algorithm Development group. He was also the Deputy Manager of the Climate, Oceans and Solid Earth Section from 2007 to 2009 and the Section Manager from 2009 to 2013. He served as the Project Scientist of the National Aeronautics and Space Administration (NASA) Aquarius mission from January 2012 to September 2013, the Deputy Project Scientist of the NASA Soil Moisture Active Passive (SMAP) Mission from January 2013 to September 2013, and the SMAP Project Scientist since October 2013. He has been the Principal/Coinvestigator of numerous NASA and Department of Defense research projects on remote sensing of soil moisture, terrestrial snow, ocean salinity, and ocean wind. He has authored four book chapters and authored or coauthored more than 150 publications and presentations.

Dr. Yueh was the recipient of the IEEE Geoscience and Remote Sensing Society Transaction Prize Paper Award in 1995, 2002, 2010, and 2014. He also received the 2000 Best Paper Award in the IEEE International Geoscience and Remote Symposium. He received the JPL Lew Allen Award in 1998 and the Ed Stone Award in 2003. He received the NASA Exceptional Technology Achievement Medal in 2014. He is the Editor-in-Chief of IEEE TRANSACTIONS ON GEOSCIENCE AND REMOTE SENSING.

Alexander G. Fore received the A.B. degree from Vassar College, Poughkeepsie, NY, USA, in 2002, and the M.S. and Ph.D. degrees from Carnegie Mellon University, Pittsburgh, PA, USA, in 2004 and 2008, respectively, all in physics.

His doctoral work was modeling of complex fluids using the lattice Boltzmann method. In March 2008, he joined the Radar Science and Engineering Section, Jet Propulsion Laboratory (JPL), California Institute of Technology, Pasadena, CA, USA. At JPL, he has been working primarily on scatterometry, both forward modeling of the radar observation as well as retrieval of the geophysical quantity from the radar observation. He also has experience in synthetic aperture radar processing and calibration algorithms.

Akiko Hayashi received the B.S. degree in civil engineering and the M.S. degree in structural engineering from Duke University, Durham, NC, USA.

After graduating, she joined the Structures and Dynamics Technology Group, Jet Propulsion Laboratory (JPL), California Institute of Technology, Pasadena, CA, USA, where she was engaged in structural analysis and finite element modeling. In 1988, she moved to the Oceanography Group and worked on altimetry data. She is currently a member of the Oceans and Ice Group, JPL, working o altimetry data from Ocean Surface Topography Mission/Jason-2, ocean salinity data from Aquarius, and soil moisture active passive data.

Michael Steele received the B.A. degree in physics from Reed College, Portland, OR, USA, in 1981, and the Ph.D. degree in geophysical fluid dynamics from Princeton University, Princeton, NJ, USA, in 1987.

Since 1987, he has worked as an Oceanographer at the Polar Science Center, Applied Physics Laboratory, University of Washington, Seattle, WA, USA. His focus is on the physical oceanography and sea ice of the Arctic Seas, with a recent interest in ocean surface change in response to and as forcing for sea ice change. He runs the UpTempO buoy project, which deploys ocean surface drifters to document change in the Seasonal Ice Zone, the area between the maximum winter and minimum summer sea ice extents.